APPLIED PHYSICS LETTERS **99**, 221106 (2011)

Experimental realization and modeling of a subwavelength frequency-selective plasmonic metasurface

Ping-Chun Li, Yang Zhao, Andrea Alù, and Edward T. Yu[a)]
Microelectronics Research Center, University of Texas at Austin, 10100 Burnet Rd., Austin, Texas 78758, USA

(Received 7 September 2011; accepted 5 November 2011; published online 29 November 2011)

We have modeled, fabricated, and characterized a plasmonic metasurface with subwavelength features, whose dominant resonance is the independent of incident angle and polarization, and sensitive only to the material composition and geometry of a single element. Higher-order resonances, associated with surface plasmon polariton (SPP) coupling and higher diffraction orders, are sensitive to the incident angle and the array periodicity and less pronounced compared with the metasurface resonance. Numerical simulations and theoretical analysis highlight a clear physical difference between the SPP resonances and the dominant metasurface collective resonance, whose properties may be of great interest for plasmonic solar cells and subwavelength color filters. © *2011 American Institute of Physics*. [doi:10.1063/1.3664634]

In recent years, plasmonic subwavelength structures have been the subject of intense research interest for their unusual collective properties such as extraordinary optical transmission and color filtering.[1–3] In this letter, we report the design, modeling, realization, and characterization of a two dimensional array formed by subwavelength Au patches, exhibiting a strong collective electromagnetic resonance in the visible regime. This resonance is found to be sensitive only to the dimensions of the patches and insensitive to the incident angle and polarization and to the spacing between patches. Theory, simulations, and experiments have been used to explain this behavior in terms of the underlying relevant physical phenomena.

For these studies, $1 \times 1\,\text{mm}^2$ areas on a glass substrate coated with 150 nm indium tin-oxide (ITO) were patterned with two dimensional arrays of square patches using electron beam lithography. The array side length and spacing of each patch are denoted by W_d and W_s, respectively. A 30 nm-thick Au layer is deposited by electron beam evaporation, followed by a standard lift-off process to create the Au patch structure. A schematic diagram of the sample structure and experimental geometry and a scanning electron micrograph of an Au patch array are shown in Figs. 1(a) and 1(b), respectively.

Optical transmittance measurements were performed using collimated light from a halogen lamp spectrally resolved by a monochromator. The monochromatic light is linearly polarized by a Glan-Thompson polarizer before it reaches the device. The device is mounted on a rotating stage, so that measurements can be performed at different incident angles θ. Numerical simulations of the field distribution in these structures are based on rigorous coupled wave analysis (RCWA) (Refs. 4 and 5) and enhanced with modal transmission line (MTL) theory.[6] Parallel full wave numerical simulations were also performed with finite-integration software to validate the results. The material dispersion of Au and glass is modeled using the Lorentz-Drude model with published material parameters,[7] which fit well with experimental measurements.[8] The optical properties of ITO can vary due to different deposition methods, so we fit its dielectric constant from our measurements and we neglect here its weak frequency dispersion in the optical regime.

Our results can be understood using the concept of a metasurface, a periodic array of scattering elements whose dimensions and periods are small compared with the operating wavelength. These features allow for characterization in terms of dipolar polarizabilities of each scatterer. Imposition of the generalized sheet transition conditions[9,10] (GSTCs) for average electromagnetic fields across the surface allows the boundary-value problem to be solved for the dominant diffraction order. The subwavelength period of the metasurface ensures that all higher-order diffraction terms are evanescent, implying that the collective resonance of the array is weakly dependent on the angle of incidence.[11] Under this assumption, we can characterize the metasurfaces using generalized dyadic polarizabilities, which describe the level of averaged electric and magnetic polarization for applied electric and magnetic fields. We assume them to be diagonal in a suitable reference system, due to the symmetries of the metasurface elements,

$$\overleftrightarrow{\alpha}_{ES} = \alpha_{ES}^{xx}\vec{x}\,\vec{x} + \alpha_{ES}^{yy}\vec{y}\,\vec{y} + \alpha_{ES}^{zz}\vec{z}\,\vec{z}, \tag{1}$$

$$\overleftrightarrow{\alpha}_{MS} = \alpha_{MS}^{xx}\vec{x}\,\vec{x} + \alpha_{MS}^{yy}\vec{y}\,\vec{y} + \alpha_{MS}^{zz}\vec{z}\,\vec{z}. \tag{2}$$

Under this definition, the generalized polarizabilities include the coupling effects among the elements in the surface. In the limit of small periods, the polarizabilities do not depend on the angle of incidence and are dominated by the individual element response, but for larger periods, spatial dispersion effects may arise. For the simple shapes considered here (square patches), in the subwavelength limit, electric effects are expected to dominate the magnetic ones. The reflection and transmission coefficients can then be derived as a function of the electric and magnetic generalized polarizabilities. The resonance conditions leading to total reflection in the limit of zero losses may be obtained as a function of incident angle and polarization as[12]

$$k_0^2\alpha_{MS}^{xx}(\alpha_{ES}^{yy} - \alpha_{MS}^{zz}\sin^2\theta) = 4 \quad \text{for} \quad \text{TE}, \tag{3}$$

[a)]Electronic mail: ety@ece.utexas.edu.

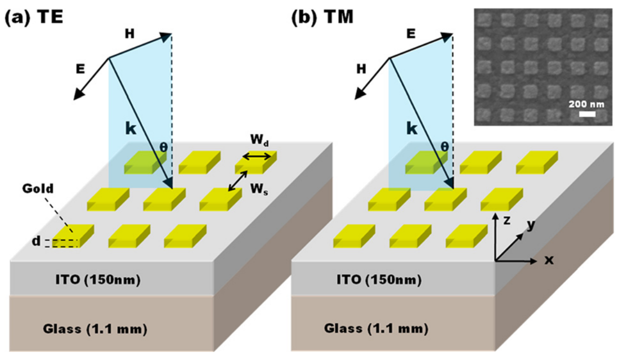

FIG. 1. (Color online) (a) and (b) Schematic diagram of the metasurface structure on an ITO coated glass substrate under illumination with TE and TM polarization, respectively. The inset shows a scanning electron micrograph of a $W_d = W_s = 200$ nm device.

$$k_0^2\alpha_{ES}^{xx}(\alpha_{MS}^{yy} - \alpha_{ES}^{zz}\sin^2\theta) = 4 \quad \text{for} \quad \text{TM}, \tag{4}$$

where k_o is the free-space wave vector, and TE and TM stand for transverse electric and transverse magnetic polarization, respectively.

The Au structures analyzed here have typical dimensions W_s, W_d of 100–200 nm and thickness of 30 nm, ensuring that the transverse components of the electric polarizability dominate the ones in the normal direction ($\alpha_{ES}^{zz} \approx 0$). For oblique TM incidence, a normal magnetic dipole moment may in principle be induced on the metasurface, even in the limit of zero thickness, but due to the simple shape of our structures, this magnetic response is expected to be negligible in the subwavelength regime. These considerations enable resonant conditions to be achieved that are weakly dependent on the incidence angle, as $\alpha_{ES}^{yy} \gg \alpha_{MS}^{zz}\sin^2\theta$ and $\alpha_{MS}^{yy} \gg \alpha_{ES}^{zz}\sin^2\theta$ in Eqs. (3) and (4).

The calculated and measured transmittance spectra for our arrays with $W_d = W_s = 100$ nm under various incident angles are shown in Fig. 2(a) for both TE and TM polarized light. The resonant dip shows clear independence of polarization and incident angle up to 60°, which is consistent with simulations and our theoretical model.

Similar experiments have been conducted with larger Au patches, $W_d = W_s = 200$ nm, as shown in Fig. 3. From both the experimental data and simulations, we notice that the main metasurface resonant dip (∼900 nm) remains unchanged under different polarization and incident angles, but is redshifted compared with the $W_d = W_s = 100$ nm device (∼680 nm), as expected due to the larger size of the individual metasurface elements.[13] In this case, the array period is still substantially smaller than the wavelength, and the polarizability model holds, yielding essentially no dependence on the incidence angle.

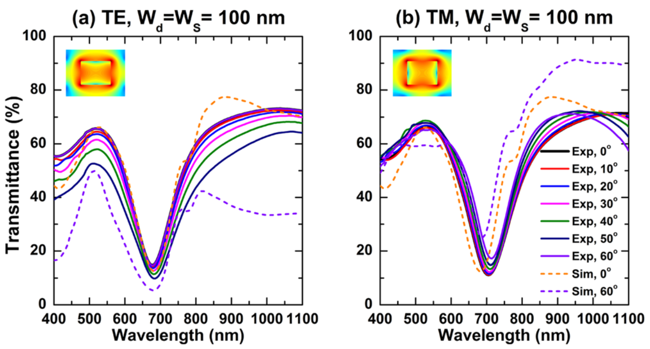

FIG. 2. (Color online) Transmission spectra of device with $W_d = W_s = 100$ nm for (a) TE and (b) TM polarization. Solid and dashed lines represent the measured and simulated spectra, respectively. The insets show the distribution of the tangential components of electrical field at the resonant wavelength, as calculated with full-wave simulations, indicating that the resonance dip is indeed due to the resonance of a single metasurface element.

In addition to the main metasurface resonance, we notice a local minimum appearing at ∼600 nm (indicated by a green arrow) for both TE and TM polarization when $\theta = 0°$ in Fig. 3. As θ increases, this local minimum starts to split into two smaller dips (indicated by solid and dashed arrows) which gradually shift away from each other. This effect is associated with the coupling of incident light with a surface plasmon polariton (SPP) supported by the grating. Conservation of momentum imposes the following condition for SPP coupling:[14]

$$\vec{k}_{SPP} = \vec{k}_{in} + m_x\vec{G}_1 + m_y\vec{G}_2, \tag{5}$$

where $k_{SPP} = (2\pi/\lambda)\sqrt{\varepsilon_{ITO}\varepsilon_{Au}(\lambda)/(\varepsilon_{ITO} + \varepsilon_{Au}(\lambda))}$ and $k_{in} = (2\pi/\lambda)\sin\theta$ are the parallel components of the wave vector of the SPP and the incident plane wave, respectively. $\vec{G}_1 = 2\pi/(W_d + W_s)\vec{x}$ and $\vec{G}_2 = 2\pi/(W_d + W_s)\vec{y}$ represent the 2D reciprocal lattice grating basis vectors, and m_x and m_y are integers corresponding to different diffraction orders. Equation (5) can be simplified to obtain

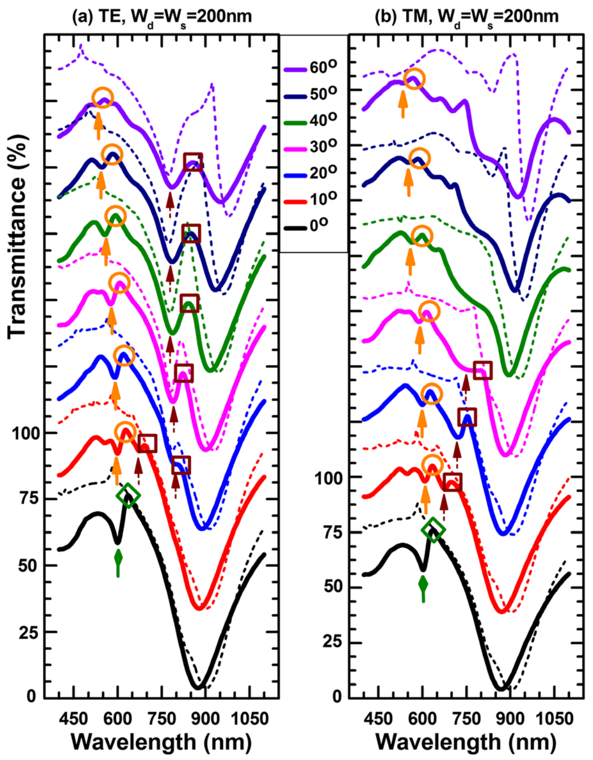

FIG. 3. (Color online) Transmission spectra of a $W_d = W_s = 200$ nm device for different incident angles with (a) TE and (b) TM polarization. Solid and dashed lines represent measured and simulated spectra, respectively. Transmission spectra at different incident angles have been offset vertically by 35% each for clarity. Different colored arrows indicate different SPP-coupled modes: diamond, (±1,0) and (0,±1); solid, (0,±1); dashed, (−1,0). Different colors of symbols indicate different orders of Wood's anomalies: diamond, (±1,0) and (0,±1); circle, (0,±1); square, (−1,0).

$$\frac{1}{\lambda}\sqrt{\frac{\varepsilon_{ITO}\varepsilon_{Au}(\lambda)}{\varepsilon_{ITO}+\varepsilon_{Au}(\lambda)}}=\sqrt{\left(\frac{\sin\theta}{\lambda}+\frac{m_x}{W_d+W_s}\right)^2+\left(\frac{m_y}{W_d+W_s}\right)^2}, \tag{6}$$

where λ is the wavelength of incident light and ε_{ITO} is the dielectric constant of ITO. TM polarization supports the same resonant wavelengths, due to the symmetries of our geometry. We have assumed the dielectric constant of ITO to be $\sim 1.91\varepsilon_0$, which is its bulk permittivity in the optical regime. We have also used experimental data for the Au permittivity.[8] To interpret our results, we examine the case of normal incidence in Figs. 3(a) and 3(b), where the local minimum originates from the grating modes (±1,0) and (0,±1). Since they are four-fold degenerate, this resonance is more pronounced compared with oblique incidence. As the incident angle becomes larger, modes (0,±1) (solid arrows) and (-1,0) (dashed arrows) are no longer degenerate, so they gradually shift apart as predicted by Eq. (6). At large incident angles ($\theta > 40°$), the SPP resonant dip remains fixed at 700 nm, due to the anti-crossing of the SPP resonance with the dominant metasurface resonance, which is not affected by the incidence angle.

Further inspection of the SPP resonances in Figs. 3(a) and 3(b) reveals that they are always accompanied by sharp transmission peaks, indicated by orange and brown circles. These are associated to Wood's anomalies[15] and can be described by replacing k_{SPP} with n_{sub}/λ in Eq. (6), where n_{sub} is the effective refractive index of the substrate. Our numerical and experimental results indicate that $n_{sub} \sim 1.6$, which is slightly higher than the refractive index of the bare ITO ($n_{ITO}=\sqrt{\varepsilon_{ITO}}=\sim 1.4$), due to the influence of the Au layer. Similar to SPP-coupled grating modes, we observe a sharper Wood's anomaly peak at $\theta = 0°$, caused by four-fold mode degeneracy compared with the spectra under non-normal incident light. The peak splits into two minor ones, and they gradually move away from each other as we increase θ; anti-crossing behavior is observed when $\theta > 40°$.

We summarize the behavior of the SPP-coupled grating modes, Wood's anomalies and metasurface resonances in the band diagrams shown in Fig. 4. Generally, the theory and experimental data are in excellent agreement for $\theta < 40°$. In the range $\theta > 40°$, the anti-crossing among the different bands shows some expected detuning, due to the dominant response of the metasurface resonance. As expected, the metasurface resonance shows a flat angular response, dominated by the metasurface element resonances, consistent with Eq. (6) and the previous discussions.

In conclusion, we have modeled, fabricated, and characterized the optical transmission spectra of two-dimensional Au patch arrays. We have examined different periodicities, which determine the properties of the metasurface resonance and of SPP-coupled grating modes. The major difference between these two resonant phenomena consists in their sensitivity to the incident angle, due to the different underlying phenomena; the collective metasurfaces resonance is based on the plasmonic resonance of an individual metasurface element and only weakly affected by the array coupling, whereas the SPP-coupled grating modes are lattice effects that are very sensitive to the incidence angle. High tolerance of incident angles and polarization in transmission and reflection of the metasurface resonance can be potentially useful for broad-angle energy harvesting applications, such as plasmonic solar cell, and for other devices, such as subwavelength plasmonic color filters.

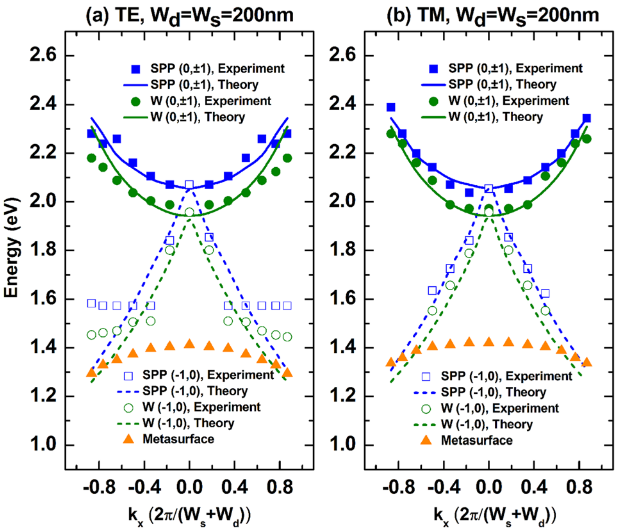

FIG. 4. (Color online) Band diagrams extracted from theoretical and measured spectral feature for SPP-coupled grating modes, Wood's anomaly, and metasurface resonances: (a) TE, $W_d = W_s = 200$ nm; (b) TM, $W_d = W_s = 200$ nm.

This work has been partially supported by an AFOSR YIP Grant No. FA9550-11-1-0009 and a NSF CAREER Award No. ECCS-0953311 (to A.A.), and by the Department of Energy (DE-FG36-08GO18016), the National Science Foundation (DMR1066430), and the Judson S. Swearingen Regents Chair in Engineering at the University of Texas at Austin (to E.T.Y.).

[1] T. W. Ebbesen, H. J. Lezec, H. F. Ghaemi, T. Thio, and P. A. Wolff, Nature **391**, 667 (1998).
[2] A. Christ, S. G. Tikhodeev, N. A. Gippius, J. Kuhl, and H. Giessen, Phys. Rev. Lett. **91**(18), 183901 (2003).
[3] T. Xu, Y.-K. Wu, X. Luo, and L. Jay Guo, Nat. Commun. **1**, 59 (2010).
[4] M. G. Moharam and T. K. Gaylord, J. Opt. Soc. Am. A **3**(11), 1780 (1986).
[5] L. Li, J. Opt. Soc. Am. A **14**(12), 2758 (1997).
[6] C.-H. Lin, K. Ming Leung, and T. Tamir, J. Opt. Soc. Am. A **19**(12), 2005 (2002).
[7] A. D. Rakic, A. B. Djurilic, J. M. Elazar, and M. L. Majewski, Appl. Opt. **37**(22), 5271 (1998).
[8] E. D. Palik, *Handbook of Optical Constants of Solids* (Academic, New York, 1991).
[9] E. F. Kuester, M. A. Mohamed, M. Piket-May, and C. L. Holloway, IEEE Trans. Antennas Propag. **51**(12), 2641 (2003).
[10] C. L. Holloway, M. A. Mohamed, E. F. Kuester, and A. Dienstfrey, IEEE Trans. Electromagn. Compat. **47**(6), 853 (2005).
[11] H. Mosallaei and K. Sarabandi, IEEE Trans. Antennas Propag. **52**(9), 2403 (2004)
[12] J. A. Gordon, C. L. Holloway, and A. Dienstfrey, IEEE Antennas Wireless Propag. Lett. **8**, 1127 (2009).
[13] J. P. Kottmann and O. J. F. Martin, Opt. Lett. **26**(14), 1096 (2001).
[14] H. Raether, *Surface Plasmons on Smooth and Rough Surfaces and on Gratings* (Springer, New York, 1988).
[15] R. W. Wood, Phys. Rev. **48**(12), 928 (1935).